Singularities at load-induced moiré locking transitions in twist grain boundaries

Jin Wang [*] and Erio Tosatti [†]
International School for Advanced Studies, Via Bonomea 265, 34136 Trieste, Italy
and International Centre for Theoretical Physics, Strada Costiera 11, 34151 Trieste, Italy

(Received 23 October 2025; revised 18 January 2026; accepted 4 March 2026; published 19 March 2026)

Recent simulation work on the moiré formed by small angle crystalline twist grain boundaries (TGBs) revealed an unexpected load-induced first-order structural transition. Most likely universal, this unconventional transition drives a frictionally superlubric-to-locked transformation. It involves moiré reconstruction, with emergence of locally commensurate mini-domains, the formation of which implies broader consequences for interfacial phenomena beyond friction, which we study by nonequilibrium molecular dynamics simulations and nonequilibrium Green's function transport calculations. We show that, for small angle ($\theta \lesssim 4^\circ$) Au(111) TGBs at the critical load of a few gigapascals, the transition is accompanied by singular responses, including a sharp dip in mechanical compliance and a ≈20–30% increase of ballistic electrical resistance as well as of interfacial thermal resistance of mixed phononic and electronic origin. Both reflect the reconstruction of interlayer registry and coupling induced by the emergence of mini-domains. These structurally driven singularities provide experimentally accessible fingerprints of the transition and reveal a unified coupling between mechanical, dissipative, and transport responses at TGBs, opening alternative routes toward the active control of moiré interfacial functionalities.

DOI: 10.1103/p9f7-ftjd

I. INTRODUCTION

Twist grain boundaries (TGBs), a classic subject in crystallography and mechanics, are ubiquitous structural defects formed by a relative twist angle θ between two adjacent crystal planes. The structural and energetic properties of TGBs have long been known and characterized [1–3], particularly in fcc metals. In spite of that, their evolution under load and dynamic response to external mechanical forcing apparently remain less explored. That is especially the case when θ is small, a regime where the moiré superstructure caused by the twist is heavily "reconstructed" [4–6]. In two-dimensional (2D) moiré materials, incommensurate moiré patterns and their evolution are well studied, and known to alter dramatically all interlayer couplings—including friction with and without load [7,8], as well as thermal transport and conductance [9–11]. Surprisingly, these same properties still call for a fresh exploration of incommensurate three-dimensional (3D) crystal TGBs.

In recent work [12], we predicted a first-order load-induced structural transition to take place in small-angle Au(111) TGBs. At a load the thermodynamic equilibrium value of which at $T = 300$ K is typically $P_c \approx 2$ GPa, the moiré superstructure transforms from a triangular, mirror-symmetric network of narrow dislocations (DSs) to a distorted, mirror-symmetry-breaking state. The transition is generally of first order and thus with hysteresis depending on temperature and waiting time. In the distorted state the two facing layers in fact acquire a very different structure. In one of the two layers the zero-load AA nodes, where interlayer repulsion is maximal, are suddenly replaced by commensurate mini-domains (MDs), a 3D variant of the classic one-dimensional Aubry transition [13]. This reconstruction, through the formation of MDs, acts analogously to interlayer joints, effectively locking the originally superlubric interface and leading to a dramatic increase in friction. More fundamentally, the AA-to-MD transformation reconstructs the interlayer registry and coupling across the interface, and is therefore expected to impact a broad range of interfacial properties and responses.

We thus explore here correlated physical responses emerging at the transition, including those in mechanical compressibility, phononic and electronic thermal transport, and ballistic conductance. We choose Au(111) TGBs for our detailed study, taking advantage of gold's excellent mechanical ductility and electrical conductivity. Results for other fcc and hcp metals will be briefly discussed later. Combining classical nonequilibrium molecular dynamics (NEMD) simulations with nonequilibrium Green's function (NEGF) electronic calculations, we predict that the load-induced transition has a sharp dip in mechanical compliance and gives rise to a subsequent measurable drop of both thermal conductance and ballistic electronic conductance. Both reflect the AA-to-MD reconstruction, which abruptly modifies interlayer coupling and reshapes the stacking-area fractions that govern interfacial transport. The first-order character of the transition predicts these changes to be singular and therefore unmistakable even when weak, thereby providing multimodal experimental

[*]Contact author: jinwang@sissa.it
[†]Contact author: tosatti@sissa.it

Published by the American Physical Society under the terms of the Creative Commons Attribution 4.0 International license. Further distribution of this work must maintain attribution to the author(s) and the published article's title, journal citation, and DOI.

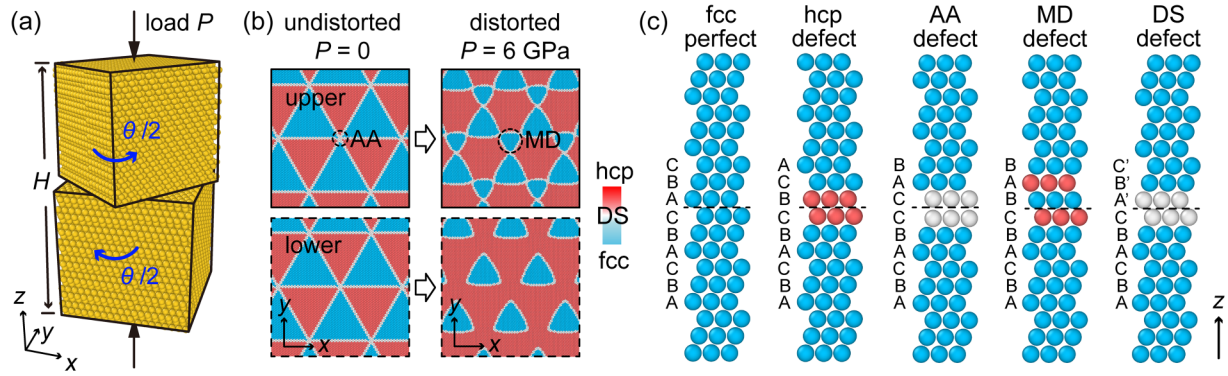


FIG. 1. Simulation model and structure. (a) Schematic diagram of a Au(111) TGB, where the upper and lower parts are rotated around z by $+\theta/2$ and $-\theta/2$. (b) Stacking configuration at the small-angle TGB interface. Upper and lower panels correspond to upper and lower surfaces. Red/blue represents hcp/fcc regions, i.e., the interfacial layers are in ABA/ABC stacking with two adjacent layers; MD indicates the locally reconstructed region replacing the original AA node; the narrow domain-wall network between neighboring commensurate regions represents the DS. For small twists, the commensurate domains extend over distances much larger than the DS width, providing a clear separation of length scales that justifies the piecewise (area-weighted) approximation used in Eqs. (4) and (6). (c) Specific stackings in different interfacial regions, including perfect fcc regions and other regions containing interfacial defects (or stacking faults), including hcp, AA, MD, and DS regions.

signatures accessible through mechanical, thermal, and electrical probes. Moreover, the likely universality of this transition across diverse 3D materials elevates it to a general mechanism governing coupled mechanical and transport responses at loaded TGB moiré interfaces.

Two necessary practical caveats are called for. First, we will display most calculations and results at the lowest possible temperatures including $T = 0$ when possible. The TGB first-order distortion and its associated effects can generally survive at finite temperatures [12]. High temperatures may promote thermally activated rotations toward $\theta = 0$, thus destroying the incommensurate twist. In practice however, edge pinning, large size, and/or external constraints can always prevent it. We therefore keep low temperature in order to obtain numerically cleaner outputs. Second, we will routinely describe results found upon increasing load. First order implies strong hysteresis at low temperatures, and we will need to reach loads as high as, e.g., 6 GPa for a spontaneous distortion, while the equilibrium transition is due at $P_c \approx 2$ GPa [12]. That too will not give problems because once distorted, the structure and its properties are essentially load independent.

II. NANOMECHANICAL SIMULATIONS

Leveraging the high computational efficiency of LAMMPS for large-scale simulations [14,15], we investigated the mechanical and thermal gradient responses of gold TGBs at small twist angles, with total atom number $\approx 10^5$. Simulation models of Au(111) TGBs consisting of $N_1 + N_2$ (111) layers containing a single twisted interface with small twist angle $\theta < 4^\circ$ were built using artificially commensurate moiré supercells satisfying periodic boundary conditions (PBC) in x and y directions. Even if commensurate, that geometry represents as usual the best approximation to incommensurability. Specifically, for each selected twist angle the supercell vectors were chosen as common lattice vectors of the two rotated Au(111) lattices [8,16]. The twist is generated by opposite rotations of slider ($N_1 = 24$) and substrate ($N_2 = 24$), $\theta/2$ and $-\theta/2$, antisymmetric against mirror reflection [Fig. 1(a)]. An embedded-atom force field [17] was used to describe the interatomic interaction; as shown earlier the results do not change with different force fields [12]. The normal load P is uniformly applied between the top layer atom of the slider and the bottom layer atom of the substrate. During the loading process, the overall stress of the model along x and y was adaptively relaxed to zero by adjusting the box size.

By gradually increasing the normal load P applied to the top and bottom layer atoms in the model, the structural transition takes place spontaneously at an instability load $P_{\rm inst} \approx 6$ GPa ($T = 0$). With the same simulation methods, the transition is also found in other systems, including fcc Ag(111) and hcp Co(111) TGBs, although at higher critical loads due to the lower ductility compared with gold. In fact, according to our previous theoretical framework [12], this Aubry-type transition, characterized by the reconstructive replacement of AA nodes with commensurate MDs [Fig. 1(b)], can be expected to occur at most twisted (111) interfaces—of course when not preempted by other transformations.

We illustrate in Fig. 1(c) the stacking at the undistorted and distorted interface, including fcc perfect regions, interfacial defects (or stacking faults) in hcp regions, DS networks, AA nodes, and MD regions. The mean interfacial repulsion across the TGB is slightly reduced once the AA nodes are replaced by MDs, leading to a drop in the overall system height H [Fig. 1(a)], which satisfies

$$H(P) = H_0(1 - P/E_{111}) - \Delta H\Theta(P - P_{\rm inst}) \qquad (1)$$

where $H_0 = (2N_L - 1)a/\sqrt{3}$ is the height at $P = 0$, $a = 4.08$ Å is the lattice constant, $E_{111} \approx 124$ GPa is Young's modulus along the [111] direction [17], ΔH is the height drop at $P_{\rm inst}$, and Θ is the Heaviside step function.

As shown in Fig. 2(a), the height drop for the $\theta = 2.88^\circ$ TGB is $\Delta H = 0.0086$ Å, or 0.36% of the interlayer spacing. Although that is tiny, the first-order nature of the structural transition still implies a delta-function singularity of

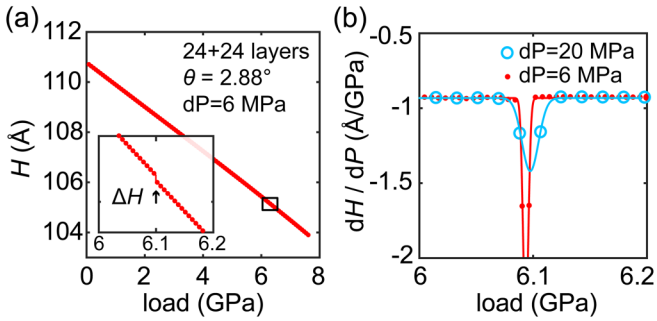


FIG. 2. (a) Dependence of system height H on increasing normal load. The inset zooms in around 6 GPa (upper end of the hysteresis cycle), showing for an arbitrarily chosen small twist angle $\theta = 2.88^\circ$ a clear height drop ΔH, accompanying the structural transformation. (b) Mechanical compliance variation as a function of increasing load. Red and blue data correspond to different loading rates.

mechanical compliance dH/dP at P_{inst}:

$$dH/dP = -H_0/E_{111} - \Delta H\delta(P - P_{\text{inst}}). \tag{2}$$

This singularity is confirmed by simulations performed under two different loading rates (with pressure increments dP of 6 and 20 MPa per step)—the simulation with the lower loading rate produces a sharper transition, as shown in Fig. 2(b). Notably, the compliance (or equivalently, stiffness) of the system remains unchanged across the structural transition, indicating robust mechanical properties that are important in practical applications.

After the response to external mechanical stimuli, we examine next the changes in thermal and electrical transport across the interface before and after the transition, from both electronic and phononic perspectives.

III. TGB ELECTRICAL RESISTANCE

We wish to evaluate the change of the TGB-related electrical resistance taking place at the load-induced pinning transition. If we were able to calculate the ballistic electronic conductance of the TGB interface, inclusive of its moiré pattern, we could reach our goal by means of NEGF calculations [18] in three simple steps. First, calculate the nominal ballistic conductance (per unit area) g_0 of the nontwisted interface (perfect fcc crystal). That will serve to establish the zero-resistance reference. Second, calculate for the same unit area the conductance g_u (where $g_u < g_0$) of the twisted, undistorted interface. The loss of conductance reflects the partial electron backscattering caused by the TGB, the resistance of which therefore should amount to $R_u = 1/g_u - 1/g_0$ when undistorted. Third, calculate the conductance g_d of the twisted, distorted interface (after the structural transition), obtaining its TGB resistance $R_d = 1/g_d - 1/g_0$. Finally, the relative change of interfacial electric resistance $\Delta R/R$ caused by the TGB distortion is

$$\Delta R/R = \frac{R_d - R_u}{R_u} = \frac{g_u/g_d - 1}{1 - g_u/g_0} = \frac{\mathcal{T}_u/\mathcal{T}_d - 1}{1 - \mathcal{T}_u} \tag{3}$$

where $\mathcal{T}_u$ and $\mathcal{T}_d$ are the ballistic transmission probabilities across the undistorted and distorted TGB respectively, satisfying $g_u = \mathcal{T}_u g_0$ and $g_d = \mathcal{T}_d g_0$.

TABLE I. Transmission $\mathcal{T}$, reflection coefficient r, and nominal ballistic conductance (per unit area) from NEGF calculations across Au(111) interfaces with different grain boundaries, along with the perfect interface, designated as fcc.

System	fcc	hcp	AA	MD	DS
$\mathcal{T}_i(E_F)$	0.868	0.816	0.815	0.862	0.833
$r_i = \mathcal{T}_{\text{fcc}} - \mathcal{T}_i$	0	0.052	0.053	0.006	0.035
g_i ($\times 10^{14}$ S/m^2)	9.235	8.680	8.673	9.169	8.867

Operationally, the small angle moiré system contains $\approx 10^5$ atoms, far too many to attempt a full-fledged NEGF ballistic conductance calculation, be it of *ab initio* density functional theory type or even of tight binding model type. We thus resorted to a simple model estimate, inspired by a piecewise approximation the order-of-magnitude validity of which will also be verified later in the phononic case.

We constructed unit model structures separately corresponding to fcc, hcp, AA, MD, and DS interface regions in the TGB [Fig. 1(c)]. For each model we calculated the transmission $\mathcal{T}_i$ and electrical conductance G_i using the NEGF method (details in Supplemental Material [19]), $G_i = \mathcal{T}_i(E_F)2e^2/h$. The reflection coefficient r_i can be defined, with respect to the fcc reference, as $r_i = \mathcal{T}_{\text{fcc}} - \mathcal{T}_i$. The calculated transmission, reflection coefficient, and nominal ballistic conductance per unit area $g_i = G_i/A_0$ for each interface structure are listed in Table I, where $A_0 = 7.283$ Å^2 is the area of unit model structures, as shown in Fig. 1(c). By varying the in-plane area of the simulation cell, we find that G_i scales linearly with area, thereby confirming the area independence of g_i.

We then approximate the overall interfacial conductance (per unit area) of the real TGB as the area-weighted average:

$$\bar{g} = \frac{1}{A}\sum_i^{\text{region}} A_i g_i \tag{4}$$

where A is the (twist angle-dependent) moiré area of the TGB, and A_i is the area of each region i. In practice, the area fractions A_i/A are estimated from the atomistic configurations by counting the number of interfacial atoms belonging to each region and normalizing by the total number (see Supplemental Material [19] for detailed values). In the current perpendicular to plane geometry considered here, the Au blocks on both sides of the interface are approximately equipotential in the lateral directions, so that different regions experience the same bias. Under this condition, combining the local contributions by an area-weighted average provides a reasonable approximation for the overall interfacial conductance.

For the $\theta = 1.61^\circ$ distorted Au(111) TGB, $\bar{g}_d$ is estimated to be 8.88×10^{14} S/m^2, lower by $\approx 1\%$ than $\bar{g}_u = 8.94 \times 10^{14}$ S/m^2 of the undistorted TGB. In turn, this is of course lower than $g_0 = 9.235 \times 10^{14}$ S/m^2 calculated for the perfect, untwisted fcc interface, the transmission coefficient of which is maximum. The corresponding reflection coefficients for the undistorted and distorted TGB are $r_u = (g_0 - \bar{g}_u)/g_0 = 0.0319$ and $r_d = (g_0 - \bar{g}_d)/g_0 = 0.0384$. The absolute values of the estimated TGB electrical conductances should not be taken too seriously, because of our crude neglect

of all transition regions between consecutive domains in the moiré. The relative changes caused by twist, and then by the distortion, should nonetheless be more accurate. By substituting the calculated g_0 and estimated $\bar{g}_u$ and $\bar{g}_d$ into Eq. (3), we obtain $\Delta R/R = 21.2\%$. Note that $\Delta R/R$ strictly focuses on transport across the interface. Additional bulk resistance from bulk leads, junctions, or defects in realistic devices would be in series, thus reducing the relative change caused by the interface structural transition. Nevertheless, this substantial increase of electric resistance upon transition of the TGB from the undistorted to the distorted state should still be accessible in carefully designed microscale experiments.

IV. TWO GEOMETRIES: NANOSCALE VERSUS MACROSCALE

Before proceeding to simulations and calculations of the TGB thermal resistance, it is therefore instrumental to specify two limiting geometries where thermal resistance and its changes could be addressed and also realistically measured. A nanoscale geometry (NG) is one where the length of the leads that face the TGB on both sides is smaller than both phonon and electron mean free paths. In that limit the heat transmission across both leads and grain boundary is entirely or prevalently ballistic. The electron-phonon interaction being largely ineffective at this scale, the electronic and phononic heat fluxes in the leads are not forced to equilibrate, and can evolve separately, acting as it were in parallel. The respective small temperature jumps at the TGB differ, adding to the different main phononic and electronic jumps located at the entry and exit junctions. In a macroscale geometry (MG) limit, in contrast, the junctions move to infinity and are irrelevant, because the length of the leads is larger than both the phonon and electron mean free paths. The two heat carriers, phonons and electrons, no longer decoupled, are in mutual equilibrium in the leads. There is a single well-defined heat distribution and gradient, inside which once again the ballistic TGB jump represents a very minor perturbation. Transmission and reflection of heat across the TGB, still ballistic in nature, contribute very little additional resistance, whereas heat conduction in the leads is governed by conventional macroscopic laws: Ohm, Wiedemann-Franz, and Fourier. The TGB resistance can be considered in series to that of the leads, which offer the overall bulk thermal resistance, of joint phononic and electronic origin. While the MG limit might be experimentally more accessible, the NG limit is directly amenable to computational simulation, a program we will pursue below. These NG calculations will directly yield the ballistic TGB thermal resistance parameters that serve to estimate the heat transmission and its changes not just in NG, but also in the MG regime. Importantly, the NG may offer the additional experimental sensitivity that may be called for in order to detect small changes caused by the pinning distortion.

V. NANOSCALE TGB THERMAL RESISTANCE

A. Phononic resistance (Kapitza)

To characterize the atomic thermal properties of our TGB in a nanoscale geometry, we used NEMD to probe the phononic thermal resistance across the Au(111) TGB. Following the same construction protocol as in previous nanomechanical simulations, we employed an artificially commensurate moiré supercell with PBC in x and y directions (a size-independence test is provided in the Supplemental Material [19]). Here we use a smaller twist angle $\theta = 1.61^\circ$—NEMD simulations are computationally less expensive than the quasistatic compression calculations, and the smaller angle allows a clearer visualization of the spatially resolved thermal response. Two separate Langevin thermostats, representing the heat source and sink, were applied to three (111) atomic layers, one at the top and the other at the bottom of the model [Fig. 3(a)]. The high-temperature region was maintained at $T_{\text{high}} = 100$ K, with the low-temperature region set to $T_{\text{low}} \approx 0$—a Langevin thermostat with zero stochastic noise but finite viscous damping acting as an energy sink. (Using a finite T_{low} gives essentially the same ΔT map; see Supplemental Material for details.) The damping coefficient in all NEMD simulations was set to a standard value of 0.1 ps. This setup establishes a steady-state total transmitted heat flux $J_t^p = J_i^p - J_r^p$ along $-z$, where J_i^p is the incident phonon flux and J_r^p is the flux reflected by the TGB. The reflection coefficient r_p is defined as $r_p = J_r^p/J_i^p = (J_i^p - J_t^p)/J_i^p = 1 - J_t^p/J_i^p$. The transmitted flux across the interface is related to the Kapitza conductance K via the interfacial temperature drop ΔT as $J_t^p = K\Delta T$. Combining these relations yields

$$r_p = 1 - \frac{K\Delta T}{J_i^p}. \tag{5}$$

As shown in Fig. 3(b), the approximate z-dependent temperature profile, which the NEMD simulation provides, also exhibits the two well-known jumps at the junctions with the high- and low-temperature external circuit and thermostats. Expected because the phonon mean free path λ_p is much larger than the lead length H, these jumps signal the largely (albeit not entirely) ballistic nature of the heat transport in the system's interior. A point to which we shall return later is that the magnitude of these junction-related temperature jumps controls the overall heat flux and with that the TGB ballistic jump magnitude. The latter is crucial to the sensitivity with which all pinning-induced changes can be detected. We also note that in a macroscopic MG case with z size larger than the phonon mean free path (impossible for us to simulate), the jumps will disappear and the TGB Kapitza resistance will simply add to the macroscopic, diffusive thermal resistance.

Results show a local temperature drop ΔT across all interfacial regions—including the fcc, hcp, AA, and MD regions—both before and after the load-induced TGB structural transition [Fig. 3(c)]. In all cases, the distorted structure has a higher phononic thermal resistance than the undistorted one. Spatially, the fcc regions consistently show the lowest resistance in both distorted and undistorted structures. That resistance is not strictly zero as one might have expected for a perfect interfacial fcc stacking, owing to the region's finite size—indicating a residual influence from neighboring regions. In all other regions the interface stacking is imperfect, resulting in a higher thermal resistance. Ranked from low to high, the resistance grows going from fcc to hcp, to AA, to MD regions (data in Table II). To gain a more intuitive understanding into the spatial distribution of resistance and its relation to the stacking, we further divided the 2D interface into a grid of size $\Delta x = \Delta y = 20$ Å, and

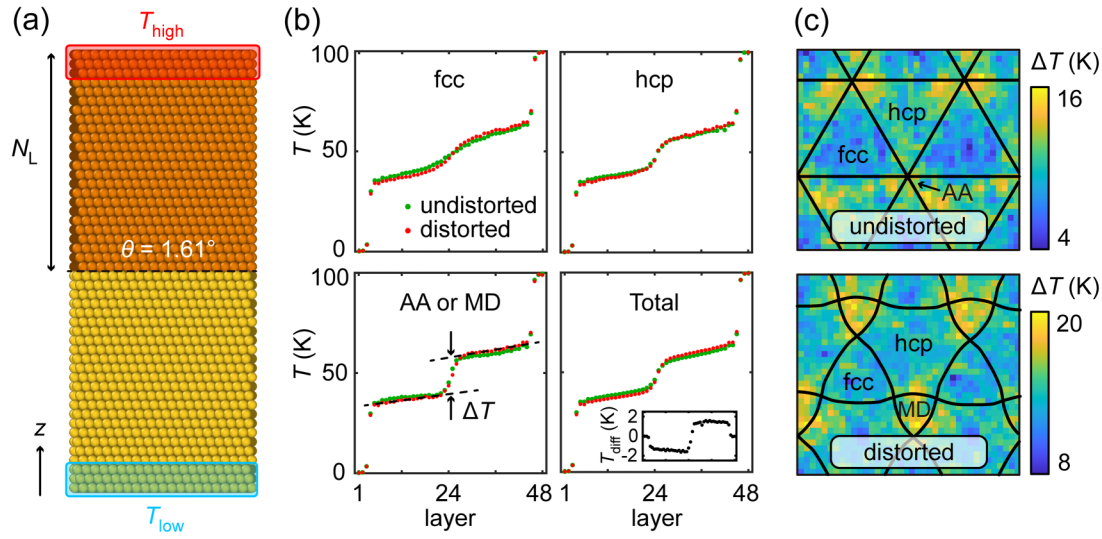


FIG. 3. Thermal conduction across a $\theta = 1.61°$ Au(111) TGB from NEMD. (a) Simulation setups, where the top and bottom three layers are coupled to hot and cold thermostats respectively. (b) Temperature profiles along the z direction within fcc, hcp, and AA or MD regions. Green and red data correspond to results before and after the transition; the inset in the lower right panel shows their difference. (c) Spatially resolved interfacial temperature drop $\Delta T(x, y)$, representative of the local thermal resistance. Upper panel, undistorted interface; lower panel, distorted interface.

evaluated $\Delta T(x, y)$ in each subregion. The resulting 2D maps are shown in Fig. 3(c), with the upper and lower panels corresponding to undistorted and distorted structure, respectively. The black curves overlaid on the map correspond to the moiré dislocation network associated with the structure [Fig. 1(b)]. The phononic Kapitza resistance R_K in this geometry directly extracted from simulations of the undistorted and distorted TGB ($\theta = 1.61°$) is $R_{K,u} = (4.97 \pm 0.09) \times 10^{-10}$ K m^2/W and $R_{K,d} = (6.49 \pm 0.10) \times 10^{-10}$ K m^2/W [Fig. 3(b)], where the error bar was estimated from three independent NEMD simulations with different temperature seeds. Therefore, if metallic electrons were absent, the distorted TGB would conduct $(R_{K,d} - R_{K,u})/R_{K,u} \approx 30\%$ less heat than the undistorted one—a very significant change.

We should note here that our simulated model, where the lead size is intermediate and the heat resistance is neither entirely ballistic nor entirely diffusive, is not necessarily suitable for comparison with a real experiment. In particular, even neglecting electronic heat flux, this NG simulation does not directly yield the results in a more general geometry. In the MG limit, where the phonon mean free path $\lambda_p \ll H$, the ballistic jumps disappear, while the overall heat resistance grows proportional to H. Due to that, the heat flux J^p_{MG} will drop like H^{-1}, whereby the grain boundary heat jump will similarly drop as $\Delta T \sim H^{-1}$. Thus their ratio and the TGB Kapitza resistance R_K, representing the phonon reflection coefficient at the TGB, must tend to a constant value. Later, we shall assume when required that the limiting macroscopic MG value of R_K is still reasonably approximated by our NG simulated result.

It is also useful and methodologically interesting to compare at this point the accurate values obtained for our model's overall phononic Kapitza resistance with an approximate, less accurate value estimated as the proportionally averaged conductances of different regions K_i, treated as was done earlier for electronic conductance [Eq. (4)], as if they conducted heat independently in parallel:

$$\bar{K} = \frac{1}{A} \sum_{i}^{\text{region}} A_i K_i. \tag{6}$$

With the value of K_i shown in Table II, the averaged Kapitza conductance and the corresponding resistance ($R_K = 1/\bar{K}$) can finally be estimated. Here we neglected the DS contribution since DS regions occupy a relatively small area fraction and their total length remains nearly unchanged before and after the transition. The Kapitza resistances obtained in this approximation for the undistorted and distorted structures are 4.05×10^{-10} and 5.65×10^{-10} K m^2/W respectively, with corresponding conductances $\bar{K} = 2.47$ and 1.77 GW/K/m^2. As shown, the piecewise-approximated phononic resistance R_K estimated from Eq. (6) is only slightly lower than the exact value, indicating that dislocations do contribute an additional but relatively small thermal resistance. The difference between $R_{K,u}$ and $R_{K,d}$ is fairly consistent with the previous accurate simulation—the phononic Kapitza resistance increases by $\approx 1.5 \times 10^{-10}$ K m^2/W, that is again about 30%, when the pinning distortion takes place. As an additional check, we performed simulations using a zero-twist

TABLE II. Temperature drop ΔT and Kapitza conductance K in each interfacial region extracted from Fig. 3(b) and estimated from Eq. (6). For the undistorted and distorted cases in Fig. 3, the transmitted heat flux is $J^p_{t,u} \approx 2.386 \times 10^{10}$ W/m^2 and $J^p_{t,d} \approx 2.295 \times 10^{10}$ W/m^2 respectively.

Region	fcc	hcp	AA	MD	Total	Eq. (6)
ΔT_{u} (K)	7.66	12.9	16.7	/	11.9	
ΔT_{d} (K)	12.6	12.7	/	18.9	14.9	
K_{u} (GW/K/m^2)	3.11	1.85	1.43	/	2.01	2.47
K_{d} (GW/K/m^2)	1.82	1.82	/	1.21	1.54	1.77

ABC-stacked system with interfacial regions of hcp and MD type [Fig. 1(c)], and for comparison, also simulated a perfect fcc system without interfacial faults. The thermal conductance calculated across these different grain boundaries confirmed that the relative ordering of phononic Kapitza resistances between different cases remains consistent with those obtained in the twisted TGB case (details in Supplemental Material [19]).

B. Electronic thermal resistance

In a metal, electrons conduct heat in addition to phonons. In good-conducting metals such as gold in particular, the electronic heat conductivity is way higher than the phononic one, especially at low temperatures [20,21]. It is therefore crucial to evaluate the additional change of electronic thermal resistance across the TGB pinning transition.

As in the above phononic case, we can do that in the NG nanoscale geometry. Because the electron mean free path in gold exceeds the nanoscale by far, the NG heat conductivity is entirely ballistic, controlled by the TGB. Since moreover the Wiedemann-Franz connection between electrical and thermal conductivity remains valid in the ballistic case [22–24], the NEGF electron reflection coefficient calculated in the earlier section directly provides the result. Laying it out in terms of the heat flux J^e, the TGB reflects a fraction of that flux, which we suppose to be small, $J^e_r \sim r_e J^e = (\mathcal{T}_{\rm fcc} - \mathcal{T})J^e$.

VI. OVERALL THERMAL RESISTANCE CHANGE

A. Nanoscale geometry

Following the above discussion, in NG there are two parallel heat fluxes so that the total flux is $J^{p+e} = J^p_i + J^e$, all phenomena caused by electron-phonon interactions being neglected. The TGB reflects a fraction, supposed to be small, of the overall flux

$$J^{p+e}_r = r_p J^p_i + r_e J^e \tag{7}$$

which then defines an overall reflection coefficient $r_{p+e} = J^{p+e}_r / J^{p+e}$. In this expression, r_p and J^p_i are directly provided by the NEMD simulation [Eq. (5)] r_e by the NEGF calculation. The electronic heat current J^e however depends on further details. By virtue of the Wiedemann-Franz law, the heat current is approximately proportional to the electric current upon application of a voltage V to the same ideal NG setup circuit where we simulated phonon heat transport. The entry and exit junctions, of resistances ρ_i and ρ_o, are decoupled from and thus in series with the TGB. Excluding electron-phonon scattering events, the voltage partition will have a first drop $\rho_i I$ at entry, a small ballistic drop $G^{-1}I$ at the TGB (of ballistic conductance G), and a final drop $\rho_o I$ at exit. Therefore $I = V/(\rho_i + \rho_o + G^{-1})$, and in conclusion

$$J^e = \frac{L_0 T}{A_0} \frac{T_{\rm high} - T_{\rm low}}{\rho_i + \rho_o + G^{-1}}, \tag{8}$$

where L_0 is the Lorenz number and T is the temperature. The two equations above determine the overall heat flux reflection coefficient for the NG case. The electronic flux is largely determined by the entry and exit resistances, which are system-specific parameters. Controlling these resistances will allow tuning the relative contributions of electronic and phononic heat conduction.

For a quantitative idea about the change of thermal conductance caused by the pinning transition, we plug in actual numbers from thermal NEMD simulations and NEGF calculations in the particular case of $\theta = 1.61^\circ$. The phononic heat flux extracted from the simulation is $J^p_i = 2.69 \times 10^{10}$ W/m^2. By substituting the remaining simulation results from Table II, in particular the purely phononic Kapitza resistances, respectively $R_{K,u} \approx 4.97 \times 10^{-10}$ K m^2/W and $R_{K,d} \approx 6.49 \times 10^{-10}$ K m^2/W for undistorted and distorted TGBs, into Eq. (7), the phononic reflection coefficients are calculated to be $r_{p,u} = 0.111$ for the undistorted TGB and $r_{p,d} = 0.147$ for the distorted TGB. The NG electronic reflection coefficient estimates provided by the NEGF calculations are on the other hand much smaller, $r_{e,u} = 0.0319$ and $r_{e,d} = 0.0384$ for the undistorted and distorted TGB ($\theta = 1.61^\circ$) respectively. Finally, we need to specify the electronic heat current J^e, which depends on the entry and exit junction resistances ρ_i and ρ_o. Inserting arbitrarily $\rho_i = \rho_o = G_0^{-1} \approx 12.9$ kΩ, we would get $J^e = 4.33 \times 10^{10}$ W/m^2, to be compared with the phononic heat current 2.69×10^{10} W/m^2. That yields $r_u = 0.0622$ and $r_d = 0.080$, a 28.6% change upon transition. Using instead very resistive junctions, e.g., $\rho_i = \rho_o = 100\, G_0^{-1}$, the thermal resistance and its changes would be dominated by phonons, with $J^e = 6.46 \times 10^8$ W/m^2, $r_u = 0.109$, and $r_d = 0.144$, a 32% change. If in contrast $\rho_i = \rho_o \ll G_0^{-1}$, the electronic conductances will dominate, and $r_u = 0.0319$ and $r_d = 0.0384$—still a ≈20% change.

B. Macroscale geometry

In macroscale crystal of length H, larger than the diffusional phonon and electron mean free paths, the phononic and electronic heat fluxes are $J^p = \kappa_p \nabla T$ and $J^e = \kappa_e \nabla T$, where κ_p and κ_e are the respective macroscopic heat conductivities. Once a TGB is inserted, it gives rise to a small reflected flux $J^{p+e}_r = r_p J^p + r_e J^e$, where we will assume that the ballistic phonon and electron reflection coefficients are equal to those calculated at the nanoscale. The total reflection coefficient for the full flux is therefore

$$r_{p+e} = \frac{r_b \kappa_p + r_e \kappa_e}{\kappa_p + \kappa_e}. \tag{9}$$

The denominator is the total, experimentally measured heat conductivity. Estimating the numerator would require a separate knowledge of the two separate heat conductivities, not equally and accurately available. We know nonetheless that $\kappa_p \ll \kappa_e$ [20,21]. It is thus a fair approximation to neglect the phononic heat flux altogether, and conclude that $r_{p+e} \approx r_e$ in a metal macroscale TGB. For the $\theta = 1.61^\circ$ Au(111) TGB in particular, that means $r_d = 0.0384$ for the distorted case, higher by ≈20% than $r_u = 0.0319$ of the undistorted case—the same as in the nanoscale geometry with very conductive junctions.

VII. SUMMARY AND OUTLOOK

In summary, we have proposed and quantitatively demonstrated unsuspected moiré-induced behaviors and properties of twist grain boundaries—structural defects of regular 3D

crystalline solids so far considered to be totally passive. We focus on the TGB in Au(111), a case where theory and reliable simulations recently discovered a superlubric-locked, Aubry-type structural transition under increasing load and decreasing twist angle. Here we found sharp mechanical and transport anomalies, both electrical and thermal, that should accompany the transition taking place in this system at loads of order gigapascal and twist angles at and below $\approx 4^\circ$. Experimentally, these small twists can be achieved by micro- and nanomanipulation of an Au island on the Au substrate and naturally stabilized by edge pinning or, if needed, by external constraints. With this in mind, by means of custom-built NEMD simulations and NEGF calculations, we showed that electrical and thermal ballistic conductances should both sharply jump across the TGB between 20 and 30% at the transition.

Importantly, these singularities are not independent, but originate from the same mini-domain driven structural transition of the moiré interface [Fig. 1(b)], which simultaneously modifies the local stacking registry and interfacial separation (giving rise to the observed z glitch) and reshapes both electronic coupling and phonon transmission. The concurrent singularities in conductance and mechanical response should make our predictions accessible to future experiments.

By no means unique to gold, the TGB locking transition and the accompanying singularities can potentially take place—albeit with different parameters—at twist interfaces in other 3D crystalline systems, particularly those with fcc or hcp structures. More generally, the present results expand the current sliding/pinning focus from 2D material moiré interfaces [8,25] to a broader class of materials and suggest that twist angles along with external loads can be leveraged as potential control parameters in the design of smart interfacial devices.

ACKNOWLEDGMENTS

We are indebted to M. Dalmonte and A. Rubio for their generous support, and to V. Vitale for helpful discussions. J.W. acknowledges the computing resources support from Ulysses in the International School for Advanced Studies and Leonardo hosted by Cineca.

DATA AVAILABILITY

The data that support the findings of this article are not publicly available upon publication because it is not technically feasible and/or the cost of preparing, depositing, and hosting the data would be prohibitive within the terms of this research project. The data are available from the authors upon reasonable request.

[1] J. T. M. D. Hosson and V. Vitek, Atomic structure of (111) twist grain boundaries in f.c.c metals, Philos. Mag. A **61**, 305 (1990).

[2] S. Dai, Y. Xiang, and D. J. Srolovitz, Structure and energy of (111) low-angle twist boundaries in Al, Cu and Ni, Acta Mater. **61**, 1327 (2013).

[3] S. Dai, Y. Xiang, and D. J. Srolovitz, Atomistic, generalized Peierls–Nabarro and analytical models for (111) twist boundaries in Al, Cu and Ni for all twist angles, Acta Mater. **69**, 162 (2014).

[4] H. Yoo, R. Engelke, S. Carr, S. Fang, K. Zhang, P. Cazeaux, S. H. Sung, R. Hovden, A. W. Tsen, T. Taniguchi, K. Watanabe, G.-C. Yi, M. Kim, M. Luskin, E. B. Tadmor, E. Kaxiras, and P. Kim, Atomic and electronic reconstruction at the van der Waals interface in twisted bilayer graphene, Nat. Mater. **18**, 448 (2019).

[5] N. P. Kazmierczak, M. Van Winkle, C. Ophus, K. C. Bustillo, S. Carr, H. G. Brown, J. Ciston, T. Taniguchi, K. Watanabe, and D. K. Bediako, Strain fields in twisted bilayer graphene, Nat. Mater. **20**, 956 (2021).

[6] J. Wang and E. Tosatti, Universal moiré buckling of freestanding 2D bilayers, Proc. Natl. Acad. Sci. USA **121**, e2418390121 (2024).

[7] O. Hod, E. Meyer, Q. Zheng, and M. Urbakh, Structural superlubricity and ultralow friction across the length scales, Nature (London) **563**, 485 (2018).

[8] J. Wang, A. Khosravi, A. Vanossi, and E. Tosatti, *Colloquium*: Sliding and pinning in structurally lubric 2D material interfaces, Rev. Mod. Phys. **96**, 011002 (2024).

[9] F. Yang, W. Zhou, Z. Zhang, X. Huang, J. Zhang, N. Liang, W. Yan, Y. Wang, M. Ding, Q. Guo, Y. Han, T.-H. Liu, K. Liu, Q. Zheng, and B. Song, Ultrahigh thermal conductance across superlubric interfaces in twisted graphite, Phys. Rev. Lett. **134**, 146302 (2025).

[10] E. Koren, I. Leven, E. Lörtscher, A. Knoll, O. Hod, and U. Duerig, Coherent commensurate electronic states at the interface between misoriented graphene layers, Nat. Nanotechnol. **11**, 752 (2016).

[11] S. Zhang, A. Song, L. Chen, C. Jiang, C. Chen, L. Gao, Y. Hou, L. Liu, T. Ma, H. Wang, *et al.*, Abnormal conductivity in low-angle twisted bilayer graphene, Sci. Adv. **6**, eabc5555 (2020).

[12] J. Wang and E. Tosatti, Superlubric-locked transition of twist grain boundaries in 3D crystals, Phys. Rev. Lett. **135**, 026202 (2025).

[13] M. Peyrard and S. Aubry, Critical behaviour at the transition by breaking of analyticity in the discrete Frenkel-Kontorova model, J. Phys. C **16**, 1593 (1983).

[14] S. Plimpton, Fast parallel algorithms for short-range molecular dynamics, J. Comput. Phys. **117**, 1 (1995).

[15] A. P. Thompson, H. M. Aktulga, R. Berger, D. S. Bolintineanu, W. M. Brown, P. S. Crozier, P. J. in 't Veld, A. Kohlmeyer, S. G. Moore, T. D. Nguyen, R. Shan, M. J. Stevens, J. Tranchida, C. Trott, and S. J. Plimpton, LAMMPS - a flexible simulation tool for particle-based materials modeling at the atomic, meso, and continuum scales, Comput. Phys. Commun. **271**, 108171 (2022).

[16] G. Trambly de Laissardière, D. Mayou, and L. Magaud, Localization of Dirac electrons in rotated graphene bilayers, Nano Lett. **10**, 804 (2010).

[17] S. M. Foiles, M. I. Baskes, and M. S. Daw, Embedded-atom-method functions for the fcc metals Cu, Ag, Au, Ni, Pd, Pt, and their alloys, Phys. Rev. B **33**, 7983 (1986).

[18] M. Brandbyge, J.-L. Mozos, P. Ordejón, J. Taylor, and K. Stokbro, Density-functional method for nonequilibrium electron transport, Phys. Rev. B **65**, 165401 (2002).

[19] See Supplemental Material at http://link.aps.org/supplemental/10.1103/p9f7-ftjd for additional details of NEGF calculations and NEMD simulations, which includes Refs. [18,26].

[20] G. Grimvall, *Thermophysical Properties of Materials* (Elsevier, Amsterdam, 1999).

[21] J. M. Ziman, *Electrons and Phonons: The Theory of Transport Phenomena in Solids* (Oxford University Press, New York, 2001).

[22] N. Mosso, U. Drechsler, F. Menges, P. Nirmalraj, S. Karg, H. Riel, and B. Gotsmann, Heat transport through atomic contacts, Nat. Nanotechnol. **12**, 430 (2017).

[23] L. Cui, W. Jeong, S. Hur, M. Matt, J. C. Klöckner, F. Pauly, P. Nielaba, J. C. Cuevas, E. Meyhofer, and P. Reddy, Quantized thermal transport in single-atom junctions, Science **355**, 1192 (2017).

[24] J. C. Klöckner, M. Matt, P. Nielaba, F. Pauly, and J. C. Cuevas, Thermal conductance of metallic atomic-size contacts: Phonon transport and Wiedemann-Franz law, Phys. Rev. B **96**, 205405 (2017).

[25] J. Wang and E. Tosatti, Aubry pinning transition of twisted two-dimensional material bilayers, Phys. Rev. B **112**, 155406 (2025).

[26] J. M. Soler, E. Artacho, J. D. Gale, A. García, J. Junquera, P. Ordejón, and D. Sánchez-Portal, The SIESTA method for *ab initio* order-*N* materials simulation, J. Phys.: Condens. Matter **14**, 2745 (2002).